

Magnetic-Field-Induced Transition in a Quantum Dot Coupled to a Superconductor

A. García Corral¹, D. M. T. van Zanten^{1,*}, K. J. Franke², H. Courtois¹, S. Florens¹, and C. B. Winkelmann¹

¹*Univ. Grenoble Alpes, CNRS, Grenoble INP, Institut Néel, 38000 Grenoble, France*

²*Fachbereich Physik, Freie Universität Berlin, 14195 Berlin, Germany and*

**present address: Center for Quantum Devices, Niels Bohr Institute, University of Copenhagen, and Microsoft Quantum Lab Copenhagen, Denmark*

The magnetic moment of a quantum dot can be screened by its coupling to a superconducting reservoir, depending on the hierarchy of the superconducting gap and the relevant Kondo scale. This screening-unscreening transition can be driven by electrostatic gating, tunnel coupling, and, as we demonstrate here, magnetic field. We perform high-resolution spectroscopy of subgap excitations near the screening-unscreening transition of asymmetric superconductor - quantum dot - superconductor (S-QD-S) junctions formed by the electromigration technique. Our measurements reveal a re-entrant phase boundary determined by the competition between Zeeman energy and gap reduction with magnetic field. We further track the evolution of the phase transition with increasing temperature, which is also evidenced by thermal replicas of subgap states.

The junction between a superconductor and a quantum dot displays discrete subgap energy levels called Andreev bound states (ABS) or, more specifically, Yu-Shiba-Rusinov (YSR) states when the highest occupied level hosts a single spin [1, 2]. When the antiferromagnetic exchange interaction between this spin and the leads prevails over the superconducting gap Δ , the localized spin is effectively Kondo screened, and a quasiparticle is bound at the interface. In contrast, if the exchange coupling is weaker, the superconducting condensate is marginally perturbed and the spin remains unscreened. The change between these two distinct ground states occurs via a sharp level crossing, which constitutes a simple realization of a quantum phase transition. In recent years, detailed investigations of this screening-unscreening transition have been performed, using as a control knob the variation of the level depth [3–7] or the tunnel coupling, which effectively modifies the exchange coupling strength [8–11]. The variation of an external magnetic field may provide an additional parameter with twofold consequences: increasing the magnetic field suppresses superconducting correlations (hence favoring a screened state), while the Zeeman effect enhances polarization towards one of the magnetic YSR states [5, 6, 12, 13]. Thus, the two effects associated to a magnetic field lead to a shifting of level crossing in opposite directions.

Experimentally, it is challenging to explore the effect of the magnetic field on the screening-unscreening transition, precisely for the reason that superconductivity is usually quenched before the quantum phase transition can be accessed. Hence, the quantum dot systems needs to be tuned close to the critical point using another control parameter, here the back gate voltage allowed in our transistor geometry. Furthermore, the detection of tiny level shifts between subgap states requires exquisite energy resolution in the μV range, which can be achieved only with superconducting leads.

In this Letter, we report on the observation of

the magnetic field-controlled screened-unscreened ground state transition of a quantum dot strongly coupled to one superconducting lead. An asymmetrically coupled superconductor-quantum dot-superconductor (S-QD-S) device combines the gate tunability of single electron transistors with the unprecedented spectroscopic resolution of the subgap states. Monitoring the dispersion of the subgap states allows tracking the transition between the screened and unscreened spin ground states of the quantum dot as a function of the bare level of the dot, temperature, and, most importantly, magnetic field. We use the Anderson impurity as the main framework for the modelization of our data. A general phase diagram is drawn, which demonstrates a striking re-entrant behavior of the phase boundary, due to the previously mentioned competition between Zeeman splitting and superconducting gap closing. In addition, thermal replicas of YSR states are found to emerge at finite temperature, providing an alternative yet consistent picture of the subgap spectrum.

The device fabrication process relies on controlled electromigration of an on-chip all-metallic aluminum device presenting a constriction [14]. This technique produces nanometer sized gaps and was successfully applied for connecting single molecules [15–18]. Electrostatic gate control is provided through a local metallic back gate isolated by a 18 nm thick ZrO_2 dielectric layer. Using aluminum as the constriction material, gated S-QD-S devices can thereby be formed [19–21]. Our quantum dots are colloidal gold nanoparticles of 5 nm diameter. Electromigration is performed at 4.2 K in cryogenic vacuum in a dilution cryostat. A scanning electron micrograph of an Al constriction after electromigration (without nanoparticles, for better visibility) is shown in Fig. 1a. Samples showing stable gate-dependent conductance features are further investigated at temperatures down to $T = 80$ mK. The differential conductance $G(V, V_G) = dI/dV$ is measured using the lock-in technique, as a function of bias V and gate voltage V_G . We

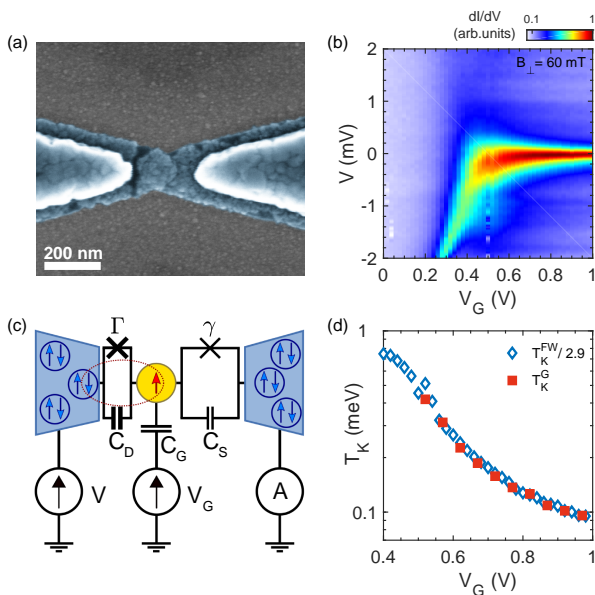


FIG. 1. (a) Scanning electron micrograph of a bare Al constriction after electromigration. (b) Normal state dI/dV differential conductance map of device A at a base temperature of $T = 100$ mK, for a magnetic field $B = 60$ mT suppressing superconductivity. (c) Schematics of the S-QD-S device, introducing the three capacitances and two tunnel couplings at play. (d) Experimental gate dependence of the Kondo energy scale T_K , determined from the temperature dependence of the linear conductance (red squares), as well as by a rescaling with a dividing factor 2.9 of the FWHM of the low-bias conductance peak (blue open diamonds).

show here data mostly from one sample, labelled A. Data from a second and similar sample (B) can be found in the Supplemental Material file.

The normal state differential conductance map (obtained at a magnetic field of 60 mT) is shown in Fig. 1b, around the only experimentally accessible degeneracy point at $V_G^0 \approx 0.40$ V. To the left, the linear conductance is suppressed, owing to a Coulomb-blockaded state with an even electron occupation number N . As the gate voltage V_G is increased, a zero-bias resonance indicates the onset of Kondo correlations associated to the spin-1/2 degeneracy of the oddly occupied $N + 1$ electron state. The electrical model of the quantum dot junction is displayed in Fig. 1c. The tunnel couplings to both leads are strongly asymmetric ($\Gamma \gg \gamma$), as evidenced by a non-unitary linear conductance limit, $G(T \rightarrow 0)/G_0 = 4\Gamma\gamma/(\Gamma + \gamma)^2 \approx 0.013$, with $G_0 = 2e^2/h$ (see Supplemental Material file). This implies notably that the Kondo resonance builds between the QD and the drain electrode at experimentally accessible temperatures, the source contact acting as a tunnel probe, as it is usually the case for the tip in an STM experiment. The following values of hybridization $\Gamma = 1.4$ meV and Coulomb repulsion $U = 12.7$ meV in the quantum dot are found from fits of the gate-dependent zero-bias conduc-

tance to Numerical Renormalization Group (NRG) calculations, see Supplemental Material. The ratio $U/\Gamma \simeq 9$ shows that the quantum dot is in the strongly correlated regime, with some deviations from Kondo scaling.

The full-width at half-maximum (FWHM) of the conduction resonance at the Fermi level, as shown in Fig. 1b, is often taken as an approximate measure of the Kondo temperature T_K , that we note T_K^{FW} (here and later we set $k_B = 1$, identifying temperature and energy scales). Another direct and precise determination of T_K is achieved considering the measured temperature dependence of the linear conductance $G(T)$. The latter can be fitted by NRG calculations, or for a lower computational cost, by an empirical expression [22, 23], leading to the gate-dependent Kondo temperature denoted T_K^G shown in Fig. 1d (see also Supplemental Material). We find that these estimates agree closely within a scaling factor, such that $T_K^G = T_K^{FW}/2.9$. Therefore, it is seen that the quantum dot junction behaves like a single spin-1/2 Kondo impurity, with a gate-tunable T_K that can be brought to the same order of magnitude as the superconducting order parameter of the leads, leading to a standard gate-control of the screening transition [24, 25].

We now turn to the study of the S-QD-S transistor at zero magnetic field. In presence of superconductivity in both leads, a transport gap of total width $2(\Delta + \Delta_{\text{probe}}) \approx 900 \mu\text{eV}$ opens in the transport map, see Fig. 2b. The Kondo peak is suppressed and two sharp symmetric resonances appear at a certain biasing voltage V so that $0 < |eV| - \Delta_{\text{probe}} < \Delta$. We take care to differentiate the gap $\Delta \approx 245 \mu\text{eV}$ of the strongly coupled lead, which governs the physical effects at play, from the gap $\Delta_{\text{probe}} \approx 205 \mu\text{eV}$ of the weakly coupled electrode, which offsets essentially the conductance onset thresholds by $\pm\Delta_{\text{probe}}$. Thermal excitations at 940 mK provide unambiguous evidence of the probe's gap size (see Fig. 4a)

The presence of the YSR states is reflected by extremely sharp subgap resonances (Fig. 2a) at $|eV| = |E_B| + \Delta_{\text{probe}}$, that is, when the probe's chemical potential allows for driving the dot to its excited state by either adding or removing an electron. The transport mechanisms leading to a d.c. current here are essentially based on Andreev processes [26]. From the experimental gate dependence of the bound state spectrum E_B , the singlet-doublet ground state transition, occurring for $E_B = 0$, is readily seen to occur near $V_G = 0.71$ V. Note that owing to the very sharply defined gap edge of aluminum [20], but also low experimental temperatures and careful shielding of the experiment, we can achieve a spectroscopic resolution down to a FWHM of less than $10 \mu\text{eV}$ (Fig. 2a), way below previously reported line widths. The latter have indeed been discussed as a lifetime limiting factor in possible subgap state-based qubits [4, 27].

Combining our knowledge of the superconducting and normal state properties, we can now plot the bound state dispersion E_B as a function of gate voltage V_G ,

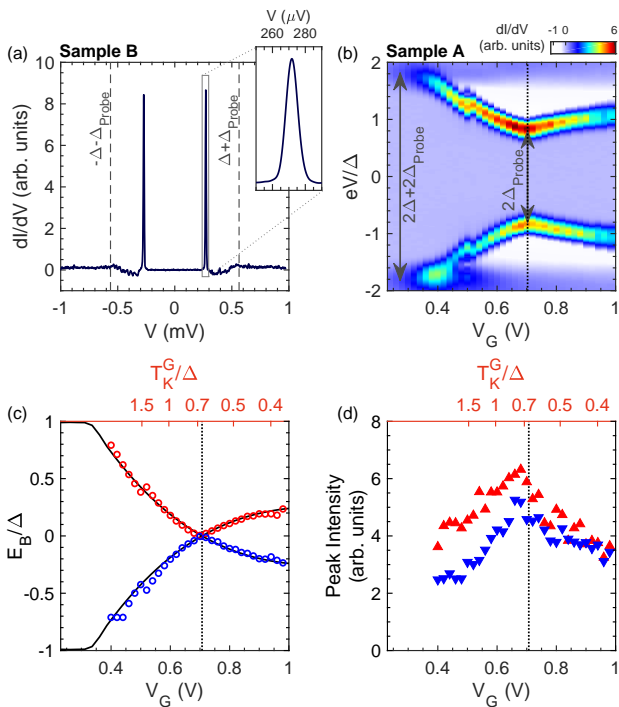


FIG. 2. (a) Differential conductance of device B measured with a lock-in AC oscillation of $2 \mu\text{V}$ in the superconducting state at fixed $V_G = 0.5 \text{ V}$, displaying very sharply resolved YSR resonances, with a FWHM = $9 \mu\text{V}$ (see inset). (b) Gate-dependent differential conductance of device A in the superconducting state at a base temperature of $T = 80 \text{ mK}$, revealing the dispersion of the YSR states. The minimal spacing of the two resonances, given by a voltage span $2\Delta_{\text{probe}}/e$ with $\Delta_{\text{probe}} = 205 \mu\text{eV}$, is associated to the quantum ground state transition, occurring at $V_G = 0.71 \text{ V}$. (c) Extracted bound state energy E_B versus gate V_G and dimensionless theoretical Kondo temperature T_K^{th}/Δ , in comparison to theoretical predictions (lines). The dashed vertical line indicates the ground state transition, found at $T_K^{\text{th}}/\Delta \approx 0.26$. (d) Evolution of the conductance peak intensities with V_G , showing a kink at the transition, consistent with a sharp un-screening transition.

which we express as a function of the dimensionless ratio T_K^G/Δ (Fig. 2c). We find the transition to the unscreened ground state for the critical value $(T_K^G/\Delta)_c \simeq 0.7$, consistent with Ref. [28] or with the value $(T_K^{FW}/2\Delta)_c \simeq 1.0$ in Ref. [29]. Theoretical calculations [24] predict a critical value $(T_K^{\text{th}}/\Delta)_c \simeq 0.30$, using the scaling formula $T_K^{\text{th}} \simeq 0.28\sqrt{U\Gamma} \exp[\pi\epsilon_0(\epsilon_0 + U)/(2\Gamma)]$. While we can rescale our data to T_K^{th} (for instance at the value at the center of the diamond), which gives a reasonable value $(T_K^{\text{th}}/\Delta)_c \simeq 0.26$, we emphasize that our device is not strictly in the scaling regime where these predictions apply quantitatively [30]. In addition, a calculation using renormalized ABS theory [31] allows us to obtain a full gate-dispersion of the bound state in good agreement with the experimental observation, see Fig. 2c and Supplemental Material file for details. Furthermore,

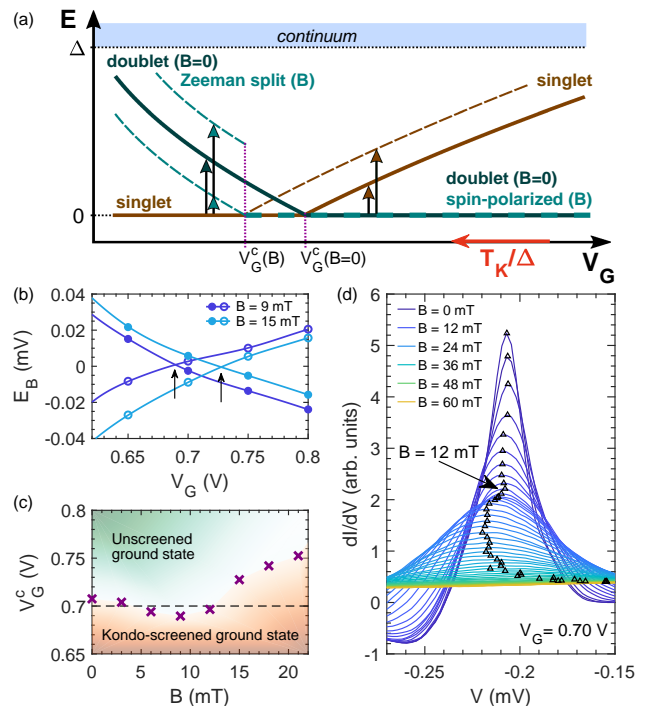


FIG. 3. (a) Sketch of the level structure of YSR states at zero magnetic field (continuous lines) and finite (dashed lines) magnetic field, in vicinity of the ground state transition. (b) Zoom on the zero-energy field crossings of the bound states dispersion for two magnetic field values, $B = 9$ and 15 mT (symbols). The solid lines are a spline interpolation of the data, from the crossing of which the value of the critical gate voltage V_G^c is determined (arrows). (c) Phase diagram of the screening transition in (V_G, B) space, showing a re-entrant phase boundary. (d) Spectroscopic analysis of the YSR states as a function of bias and at a fixed gate voltage of $V_G = 0.70 \text{ V}$, close to the zero field critical point at $V_G^c = 0.71 \text{ V}$. By increasing the magnetic field, a sharp kink is seen indicating the re-entrant phase boundary at $B = 12 \text{ mT}$.

the intensities of the conductance peaks, which reflect the weights carried by bound states, also follow the expected behaviour [24] across the ground state transition, as shown in Fig. 2d.

Having understood in detail the zero-field properties of the QD-S hybrid, we now move to the main result of this work, in which we evidence the competition of two magnetic effects on the ground state transition of the quantum dot. A magnetic field B is expected to Zeeman split the two spin projections of the doublet state by $E_Z = \pm g\mu_B B/2$, with g the gyromagnetic factor and μ_B the Bohr magneton. The effect of the Zeeman splitting on the doublet state has been observed in superconductor - quantum dot junctions formed in semiconducting nanowires, owing to the large $g \sim 20$ in these materials [5, 6, 12]. In these works, the sub-gap resonances are Zeeman split at the singlet ground state phase because two excited states are accessible. In contrast, when the

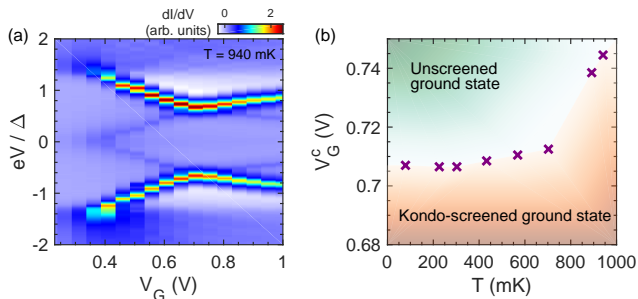


FIG. 4. (a) Differential conductance of device A in the superconducting state at the higher temperature $T = 940$ mK, displaying the YSR resonances and their thermal replicas. (b) Gate dependence of the YSR states at 940 mK, as found from the main conductance resonances (similar data is found from the thermal replicas). Owing to the temperature-driven reduction of the superconducting gap Δ , the ground state transition has moved to the larger critical gate voltage $V_G^c \approx 0.74$ V at the largest measured temperature.

singlet is the excited state, no splitting was seen, because the only possible transition (at low temperature $T < E_Z$) is from the lower energy spin-polarized state to the singlet.

Beyond the mere spectroscopic effect of the Zeeman splitting of the doublet excited state at a given dot level depth, we now consider the magnetic field effect on the ground state transition itself. Indeed, as one of the spin projections of the unscreened spin state has a lower energy, the screened ground state phase space gradually shrinks, which is translated here into a critical value of V_G moving to lower values. This is sketched in Fig. 3a and precisely observed in Fig. 3c, where we plot the critical gate value V_G^c associated to the ground state transition as a function of magnetic field. The latter is determined as previously from the kink (crossing) in the YSR dispersion, for each applied magnetic field as shown in Fig. 3b. For small fields $B < 10$ mT, there is a clear downward trend of V_G^c , indicating a Zeeman-driven reduction of the parameter space associated to the singlet ground state. As the magnetic field is further increased, the reduction of the superconducting gap starts coming into play, with a quadratic magnetic field dependence of the gap to lowest order [32]. Intuitively, the gradual weakening of superconductivity favors Kondo screening of the spin in the dot, and thereby favors the singlet ground state, enhancing again the critical V_G^c (Fig. 3c). This re-entrance of the phase-boundary is confirmed when sweeping the magnetic field at a fixed gate voltage $V_G = 0.70$ V (Fig. 3d). The transition of the ground state parity induced near a field of 12 mT is accompanied by an abrupt change in the YSR spectra, which move to higher energies and acquire a broader lineshape (see Supplemental Material file for details).

For completeness, we finally focus on the effect of higher temperatures for the tunnelling spectroscopies as

well as the ground state transition. First, at higher temperatures, the non-zero probability of finding the dot in its excited state allows for new conductance resonances in tunneling spectroscopies emerging at $|eV| = \Delta_{\text{probe}} - |E_B|$, which are commonly referred to as *thermal replicas* of the YSR resonances. This is readily seen as a pair of new peaks at low voltages in Fig. 4a. The corresponding values of the bound state energy E_B can now also be deduced from the related supplementary threshold conditions, in excellent agreement with the bound state energies deduced from the *main* resonances, leading to the data shown in Fig. 4b. The singlet-doublet transition can thus be equally observed from the thermal replicas. Second, the thermal weakening of the superconducting gap provides another method for tuning the singlet-doublet ground state transition. At $T = 940$ mK, we indeed find that the transition has moved to a larger gate value, about $V_G^c \simeq 0.74$ V (or equivalently at a lower T_K than for the base temperature), in agreement with expectations. Obviously, no re-entrance is observed in the temperature dependence of the transition.

In conclusion, we have demonstrated a magnetic field tuning of the screening-unscreening transition of a quantum dot coupled to superconductors in a transistor geometry. A novel phase diagram was established, demonstrating that the magnetic field leads to a re-entrant transition due to the competition between Zeeman stabilisation of the lowest spin-polarised orbital and weakening of the superconducting gap. A complementary finite temperature phase diagram was drawn, that reflects the sole thermal weakening on the superconducting gap, while signatures of the ground state transition were also observed in thermally excited replicas. These results demonstrate that quantum dots constitute a rich model system for the controlled exploration of strong correlations effects in nanostructures. Further developments will address the influence of the screening-unscreening transition on operational properties of single electron turnstiles [21].

This work was funded by the joint ANR-DFG grant JOSPEC and the Labex LANEF programme. Samples were fabricated at the Nanofab facility at Institut Néel-CNRS and PTA-CEA. We thank D. Basko, J. Pekola, N. Hatter and B. Heinrich for useful discussions.

-
- [1] A. V. Balatsky, I. Vekhter, and J.-X. Zhu, “Impurity-induced states in conventional and unconventional superconductors,” *Rev. Mod. Phys.* **78**, 373–433 (2006).
 - [2] B. W. Heinrich, J. I. Pascual, and K. J. Franke, “Single magnetic adsorbates on s-wave superconductors,” *Prog. Surf. Sci.* **93**, 1–19 (2018).
 - [3] R. S. Deacon, Y. Tanaka, A. Oiwa, R. Sakano, K. Yoshida, K. Shibata, K. Hirakawa, and S. Tarucha,

- “Tunneling spectroscopy of Andreev energy levels in a quantum dot coupled to a superconductor,” *Phys. Rev. Lett.* **104**, 076805 (2010).
- [4] J.-D. Pillet, C. H. L. Quay, P. Morfin, C. Bena, A. Levy Yeyati, and P. Joyez, “Andreev bound states in supercurrent-carrying carbon nanotubes revealed,” *Nat. Phys.* **6**, 965–969 (2010).
- [5] E. J. H. Lee, X. Jiang, M. Houzet, R. Aguado, C. M. Lieber, and S. De Franceschi, “Spin-resolved Andreev levels and parity crossings in hybrid superconductor–semiconductor nanostructures,” *Nat. Nanotechnol.* **9**, 79 (2014).
- [6] A. Jellinggaard, K. Grove-Rasmussen, M. H. Madsen, and J. Nygård, “Tuning Yu-Shiba-Rusinov states in a quantum dot,” *Phys. Rev. B* **94**, 064520 (2016).
- [7] A. Assouline, C. Feuillet-Palma, A. Zimmers, H. Aubin, M. Aprili, and J.-C. Harmand, “Shiba bound states across the mobility edge in doped InAs nanowires,” *Phys. Rev. Lett.* **119**, 097701 (2017).
- [8] K. J. Franke, G. Schulze, and J. I. Pascual, “Competition of superconducting phenomena and Kondo screening at the nanoscale,” *Science* **332**, 940–944 (2011).
- [9] J. O. Island, R. Gaudenzi, J. de Bruijckere, E. Burzurí, C. Franco, M. Mas-Torrent, C. Rovira, J. Veciana, T. M. Klapwijk, R. Aguado, and H. S. J. van der Zant, “Proximity-induced Shiba states in a molecular junction,” *Phys. Rev. Lett.* **118**, 117001 (2017).
- [10] L. Farinacci, G. Ahmadi, G. Reece, M. Ruby, N. Bogdanoff, O. Peters, B. W. Heinrich, F. von Oppen, and K. J. Franke, “Tuning the coupling of an individual magnetic impurity to a superconductor: quantum phase transition and transport,” *Phys. Rev. Lett.* **121**, 196803 (2018).
- [11] L. Malavolti, M. Briganti, M. Hänze, G. Serrano, I. Cimatti, G. McMurtrie, E. Otero, P. Ohresser, F. Totti, M. Mannini, R. Sessoli, and S. Loth, “Tunable spin-superconductor coupling of spin 1/2 vanadyl phthalocyanine molecules,” *Nano Letters* **18**, 7955–7961 (2018).
- [12] S. Li, N. Kang, P. Caroff, and H.Q. Xu, “ $0-\pi$ phase transition in hybrid superconductor–InSb nanowire quantum dot devices,” *Phys. Rev. B* **95**, 014515 (2017).
- [13] L. Cornils, A. Kamlapure, L. Zhou, S. Pradhan, A. A. Khajetoorians, J. Fransson, J. Wiebe, and R. Wiesendanger, “Spin-resolved spectroscopy of the Yu-Shiba-Rusinov states of individual atoms,” *Phys. Rev. Lett.* **119**, 197002 (2017).
- [14] H. Park, A. K. L. Lim, A. P. Alivisatos, J. Park, and P. L. McEuen, “Fabrication of metallic electrodes with nanometer separation by electromigration,” *Appl. Phys. Lett.* **75**, 301–303 (1999).
- [15] H. Park and P. L. McEuen, “Nano-mechanical oscillations in a single-C₆₀ transistor,” *Nature* **407**, 57–60 (2000).
- [16] J. Park, A. N. Pasupathy, J. I. Goldsmith, C. Chang, Y. Yaish, J. R. Petta, M. Rinkoski, J. P. Sethna, H. D. Abruña, and P. L. McEuen, “Coulomb blockade and the Kondo effect in single-atom transistors,” *Nature* **417**, 722–725 (2002).
- [17] W. Liang, M. P. Shores, M. Bockrath, J. R. Long, and H. Park, “Kondo resonance in a single-molecule transistor,” *Nature* **417**, 725–729 (2002).
- [18] R. Vincent, S. Klyatskaya, M. Ruben, W. Wernsdorfer, and F. Balestro, “Electronic read-out of a single nuclear spin using a molecular spin transistor,” *Nature* **488**, 357 (2012).
- [19] C. B. Winkelmann, N. Roch, W. Wernsdorfer, V. Bouchiat, and F. Balestro, “Superconductivity in a single-C₆₀ transistor,” *Nat. Phys.* **5**, 876–879 (2009).
- [20] D. M. T. van Zanten, F. Balestro, H. Courtois, and C. B. Winkelmann, “Probing hybridization of a single energy level coupled to superconducting leads,” *Phys. Rev. B* **92**, 184501 (2015).
- [21] D. M. T. van Zanten, D. M. Basko, I. M. Khaymovich, J. P. Pekola, H. Courtois, and C. B. Winkelmann, “Single quantum level electron turnstile,” *Phys. Rev. Lett.* **116**, 166801 (2016).
- [22] D. Goldhaber-Gordon, H. Shtrikman, D. Mahalu, D. Abusch-Magder, U. Meirav, and M. A. Kastner, “Kondo effect in a single-electron transistor,” *Nature* **391**, 156–159 (1998).
- [23] B. Dutta, D. Majidi, A. García-Corral, P. A. Erdman, S. Florens, T. A. Costi, H. Courtois, and C. B. Winkelmann, “Direct probe of the Seebeck coefficient in a Kondo-correlated single-quantum-dot transistor,” *Nano Lett.* **19**, 506–511 (2019).
- [24] J. Bauer, A. Oguri, and A. C. Hewson, “Spectral properties of locally correlated electrons in a Bardeen–Cooper–Schrieffer superconductor,” *J. Phys.: Condens. Matter* **19**, 486211 (2007).
- [25] R. Maurand, T. Meng, E. Bonet, S. Florens, L. Marty, and W. Wernsdorfer, “First-Order $0-\pi$ Quantum Phase Transition in the Kondo Regime of a Superconducting Carbon-Nanotube Quantum Dot,” *Phys. Rev. X* **2**, 011009 (2012).
- [26] M. Ruby, F. Pientka, Y. Peng, F. von Oppen, B. W. Heinrich, and K. J. Franke, “Tunneling Processes into Localized Subgap States in Superconductors,” *Phys. Rev. Lett.* **115**, 087001 (2015).
- [27] A. Zazunov, V. S. Shumeiko, E. N. Bratus, J. Lantz, and G. Wendin, “Andreev level qubit,” *Phys. Rev. Lett.* **90**, 087003 (2003).
- [28] C. Buizert, A. Oiwa, K. Shibata, K. Hirakawa, and S. Tarucha, “Kondo universal scaling for a quantum dot coupled to superconducting leads,” *Phys. Rev. Lett.* **99**, 136806 (2007).
- [29] J. Bauer, J. I. Pascual, and K. J. Franke, “Microscopic resolution of the interplay of Kondo screening and superconducting pairing: Mn-phthalocyanine molecules adsorbed on superconducting Pb (111),” *Phys. Rev. B* **87**, 075125 (2013).
- [30] V. Meden, “The Anderson–Josephson quantum dot - A theory perspective,” *J. Phys.: Cond. Mat.* **31**, 163001 (2019).
- [31] T. Meng, S. Florens, and P. Simon, “Self-consistent description of Andreev bound states in Josephson quantum dot devices,” *Phys. Rev. B* **79**, 224521 (2009).
- [32] A. Anthore, H. Pothier, and D. Estève, “Density of states in a superconductor carrying a supercurrent,” *Phys. Rev. Lett.* **90**, 127001 (2003).
- [33] J. M. Thijssen and Herre S. J. Van der Zant, “Charge transport and single-electron effects in nanoscale systems,” *physica status solidi (b)* **245**, 1455–1470 (2008).
- [34] M.-S. Choi, M. Lee, K. Kang, and W. Belzig, “Kondo effect and Josephson current through a quantum dot between two superconductors,” *Phys. Rev. B* **70**, 020502 (2004).
- [35] M. R. Buitelaar, T. Nussbaumer, and C. Schönberger, “Quantum dot in the Kondo regime coupled to supercon-

- ductors,” *Phys. Rev. Lett.* **89**, 256801 (2002).
- [36] S. M. Cronenwett, T. H. Oosterkamp, and L. P. Kouwenhoven, “A tunable Kondo effect in quantum dots,” *Science* **281**, 540–544 (1998).
- [37] E. J. H. Lee, X. Jiang, R. Aguado, C. M. Lieber, S. De Franceschi, *et al.*, “Scaling of subgap excitations in a superconductor-semiconductor nanowire quantum dot,” *Phys. Rev. B* **95**, 180502 (2017).
- [38] D. Goldhaber-Gordon, J. Göres, M. A. Kastner, H. Shtrikman, D. Mahalu, and U. Meirav, “From the Kondo regime to the mixed-valence regime in a single-electron transistor,” *Phys. Rev. Lett.* **81**, 5225 (1998).
- [39] I. Affleck, J.-S. Caux, and A. M. Zagoskin, “Andreev scattering and Josephson current in a one-dimensional electron liquid,” *Phys. Rev. B* **62**, 1433–1445 (2000).
- [40] Y. Tanaka, A. Oguri, and A. C. Hewson, “Kondo effect in asymmetric Josephson couplings through a quantum dot,” *New J. Phys.* **9**, 115 (2007).
- [41] E. Vecino, A. Martin-Rodero, and A. Levy Yeyati, “Josephson current through a correlated quantum level: Andreev states and π junction behavior,” *Phys. Rev. B* **68**, 035105 (2003).
- [42] N. Wentzell, S. Florens, T. Meng, V. Meden, and S. Andergassen, “Magnetoelectric spectroscopy of Andreev bound states in Josephson quantum dots,” *Phys. Rev. B* **94**, 085151 (2016).
- [43] N. A. Court, A. J. Ferguson, and R. G. Clark, “Energy gap measurement of nanostructured aluminium thin films for single Cooper-pair devices,” *Superconductor Science and Technology* **21**, 015013 (2007).
- [44] F. Levy-Bertrand, T. Klein, T. Grenet, O. Dupré, A. Benoît, A. Bidaud, O. Bourrion, M. Calvo, A. Catalano, A. Gomez, *et al.*, “Electrodynamics of granular aluminium from superconductor to insulator: Observation of collective superconducting modes,” *Phys. Rev. B* **99**, 094506 (2019).
- [45] A. A. Shanenko, M. D. Croitoru, and F. M. Peeters, “Superconducting nanofilms: Andreev-type states induced by quantum confinement,” *Phys. Rev. B* **78**, 054505 (2008).

Supplemental Information File: Magnetic-Field-Induced Transition in a Quantum Dot Coupled to a Superconductor

This supporting information discusses the sample fabrication process of electromigrated superconducting quantum dots, the electrical characterization of the Kondo-correlated quantum dot in both the normal and superconducting state, and presents a second sample showing similar physics to the one discussed in the main text. Theoretical modeling is also developed in detail, including Numerical Renormalization Group (NRG) calculations used to extract microscopic parameters of the device, as well as the determination of Andreev Bound state dispersions from renormalized perturbation theory.

SAMPLE FABRICATION

The substrates employed for the fabrication of gated electromigration junctions are 2-inch intrinsic silicon $\langle 100 \rangle$ wafers with a native oxide layer and a resistivity larger than $8000 \Omega \text{ cm}$. Three steps of lithography, followed by the corresponding metal deposition and lift-off, are carried out. First, a local back-gate is patterned by optical laser lithography using a bi-layer resist of LOR3A/S1805. After development, a deposition of 3 nm of Ti followed by 30 nm of Au is done on the sample with an electron beam evaporator and put into lift-off solvent. Then the sample surface is cleaned with a reactive ion etching oxygen plasma of 20 watts power for 5 minutes, and a ZrO_2 oxide layer of approximately 18 nm is conformally grown by atomic layer deposition (ALD) technique. In the second lithography step, the bonding pads and access lines are patterned with a hard-mask UV aligner on a LOR3A/UV3 bi-layer resist. The sample is then metallized with 3 nm of Ti plus 50 nm of Au and put into lift-off solvent. Electron-beam lithography is employed to pattern the bow-tie shaped constriction on top of the oxide-covered gate electrode in the last lithography step. A bi-layer resist of PMMA/MMA AR-P 617.06 and PMMA 3% is used to create a stable undercut by proximity effect of the beam. Suspended resist bridges at the narrowest part of the constrictions result from this undercut. By performing a double angle evaporation of 14 nm of Al fixing the sample at angles of $\pm 25^\circ$ w.r.t. the axis perpendicular to the gate electrode, nano-constrictions are grown below each undercut bridge (as shown in Fig. S5).

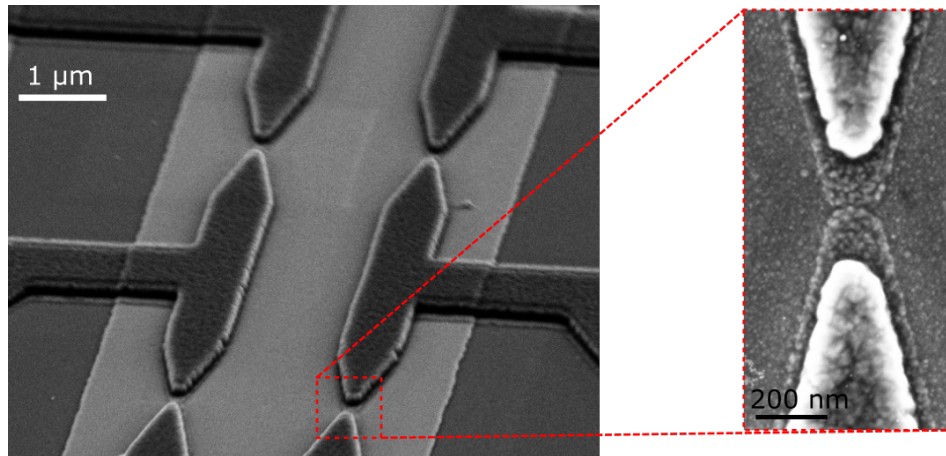


FIG. S5. Scanning electron microscope images of two Al constrictions arrays, fabricated on top of the ZrO_2 -covered gate electrode (left), and a zoom-in at a single constriction, already electromigrated (right).

The process finishes with a perpendicular evaporation of 80 nm of Al to decrease the access lines resistance. Few hundreds of individual chips are fabricated simultaneously from a 2-inch wafer, each containing 30 Al electromigration constrictions divided in two arrays. A colloidal toluene suspension of 5 nm diameter Au nano-particles (functionalized with dodecanethiol ligands) is dropcasted several times on the surface of an individual chip the same day that it is glued and bonded to a sample-holder and inserted in a dilution cryostat. Electromigration is performed inside the fridge at a cryogenic temperature of about 4 K. Junctions displaying a tunneling current with gate-dependent features are further investigated at dilution temperatures of 75 mK (increasing to 100 mK for magnetic field experiments).

Around 100 aluminum constrictions have been successfully electromigrated in the work of the present article. Several of these breaking tunnel junctions presented a gate dependent current, but only 4 displayed an identifiable diamond-like structure in the stability diagram and sub-gap current that indicated the presence of bound states. Out of 4, only 2 (samples A and B) had a gate dependence stable enough to acquire systematic successive measurements.

EXTRACTING EXPERIMENTAL PARAMETERS FROM NRG

Strongly correlated quantum dots are generically described by a single-level impurity model involving two electrodes (left/right, or drain/source), according to the Anderson Hamiltonian:

$$H = \sum_{\sigma} \epsilon_0 d_{\sigma}^{\dagger} d_{\sigma} + U d_{\uparrow}^{\dagger} d_{\uparrow} d_{\downarrow}^{\dagger} d_{\downarrow} + \sum_{k\alpha\sigma} \epsilon_k c_{k\alpha\sigma}^{\dagger} c_{k\alpha\sigma} + \sum_{k\alpha\sigma} t_{\alpha} (c_{k\alpha\sigma}^{\dagger} d_{\sigma} + \text{H.c.}), \quad (\text{S1})$$

assuming that confinement is strong enough to disregard fully occupied or empty orbitals. Here d_{σ}^{\dagger} creates an electron on the dot with spin $\sigma = (\uparrow, \downarrow)$, and $c_{k\alpha\sigma}^{\dagger}$ an electron in the lead $\alpha = (L, R)$ with spin σ and momentum k . The parameters of the model in Eq. (S1) are the single-particle energy level ϵ_0 of the quantum dot (relative to the equilibrium Fermi level of the leads, taken as energy reference), the local Coulomb repulsion U on the dot, the kinetic energy $\epsilon_{k\sigma}$ of the lead electrons, and the tunneling amplitude t_{α} from the dot to electrode α . Taking into account a generic asymmetry between the coupling to each electrode, we define the respective hybridizations as $\Gamma = \pi\rho_0(t_L)^2$ and $\gamma = \pi\rho_0(t_R)^2$, with ρ_0 the electronic density of states at the Fermi level (assumed identical in both electrodes, without loss of generality). Typically, in a tunneling geometry relevant for the present experiment, one has $\Gamma \gg \gamma$. In addition, a voltage bias $V = \mu_L - \mu_R$, originating from an imbalance of the chemical potentials μ_{α} in each lead, allows to drive a current through the nanostructure, and forms the basis of conductance measurements in electronic quantum dot devices.

We define a bonding orbital $c_{k\sigma}^{\dagger} = \sum_{\alpha} (t_{\alpha} / \sqrt{t_L^2 + t_R^2}) c_{k\alpha\sigma}^{\dagger}$ and its corresponding orthonormal antibonding orbital, so that the antibonding orbital decouples from the tunneling process via the dot level. The total hybridization of the d -level is thus $\Gamma + \gamma \simeq \Gamma$, since $\Gamma \gg \gamma$ in a tunneling geometry. This allows to use a single channel Anderson model in equilibrium, which simplifies the numerical simulations. A Kondo resonance in the dot density of states $\rho(\omega)$ develops provided $U \gtrsim \pi\Gamma$ in the local moment regime $|\epsilon_0 + U/2| \lesssim U/2$ where charge dynamics is frozen by Coulomb blockade, but spin fluctuations associated to the dot orbital assist transport through the nanostructure. One defines also the mixed valence regime between the empty and single occupied quantum dot as $|\epsilon_0| \lesssim \Gamma$.

The most crucial microscopic parameter of Hamiltonian in Eq. (S1) to be extracted from the experiment is the ratio U/Γ , which sets the strength of electronic correlations. Standard Coulomb diamond spectroscopy cannot be used in the regime where Kondo correlations are fully developed due to many-body modification of the excitations' linewidth. A more reliable method is to use the gate dependence of the zero-bias conductance, which is readily obtained from linear response theory:

$$G(V_G) = \frac{2e^2}{h} \frac{4\pi\Gamma\gamma}{\Gamma + \gamma} \rho(\omega = 0, \epsilon_0) \simeq \frac{2e^2}{h} \frac{4\pi\gamma}{\Gamma} \rho(\omega = 0, \epsilon_0) \quad (\text{S2})$$

$$\epsilon_0 = -U/2 + \alpha_G (V_G - V_G^{\text{center}}) \quad (\text{S3})$$

with $\rho(\omega, \epsilon_0)$ the zero-temperature finite frequency density of states of the impurity level, assuming that the base temperature is well below the Kondo scale. We model in Eq. (S3) a linear relation between the level position ϵ_0 and the applied gate voltage V_G , with α_G the gate lever arm, and V_G^{center} the offset voltage corresponding to the center of the Coulomb diamond in the experiment, so that $V_G = V_G^{\text{center}}$ implies $\epsilon_0 = -U/2$ (particle-hole symmetric point). The maximum value for $G(V_G)$ allowed by Friedel sum rule is $G_0 = (2e^2/h)4\pi\gamma/(\Gamma + \gamma)^2$, a value that is attained at the center of the odd charge Coulomb diamond (namely $\epsilon_0 = -U/2$) at zero temperature. We define a rescaled dimensionless conductance $g(V_G) = G(V_G)/G_0$ that crosses over from 0 (in the empty dot regime $\epsilon_0 > 0$) to 1 (at the center of the odd charge diamond $\epsilon_0 = -U/2$). The lineshape of $g(V_G)$ is interesting to estimate correlations because it forms a flat plateau of width proportional to U , and displays a crossover on a scale of the order of $\Gamma + \gamma$. In addition, $g(V_G)$ is weakly sensitive to the electronic bandwidth, provided that it is larger than hybridization (not shown). Since $g(V_G)$ is mostly controlled by the single scale U/Γ , this ratio can be extracted precisely from a scaling analysis. A comparison of the experimental measurement to the NRG data is shown in Fig. S6. We have chosen here three values of $U/\Gamma = 0, 6, 9$, and fixed the ratio $\Gamma/D = 0.3$, where D is the half-bandwidth of the electrodes. The horizontal axis corresponds to the experimental voltage V_G , and a small charge offset artifact was removed from the experimental data in order to produce a smooth curve. This results in a small offset of the center of the Coulomb

diamond expected near $V_G^{\text{center}} = 1.1\text{V}$. Regarding the rescaling of the NRG data, we apply a similar centering to the Coulomb diamond center, $\delta\epsilon_0 = \epsilon_0 + U/2$. Then we convert the energy level to voltage from the multiplicative form $\delta V_G = \delta\epsilon_0/(-\alpha_G)$. For each NRG curve, we choose α_G so that the normalized NRG conductance $g(V_G)$ crosses the experimental points at the mid point $g = 1/2$. This allow to test the scaling form of $g(V_G)$ for various values of the parameters. We find that our experimental data are best fitted for the value $U/\Gamma = 9$. One notices a slight decrease of $g(V_G)$, below the unitary limit, in the experimental data for the largest V_G values. Such a thermal effect is expected from the finite temperature (100 mK) at which the measurements were done.

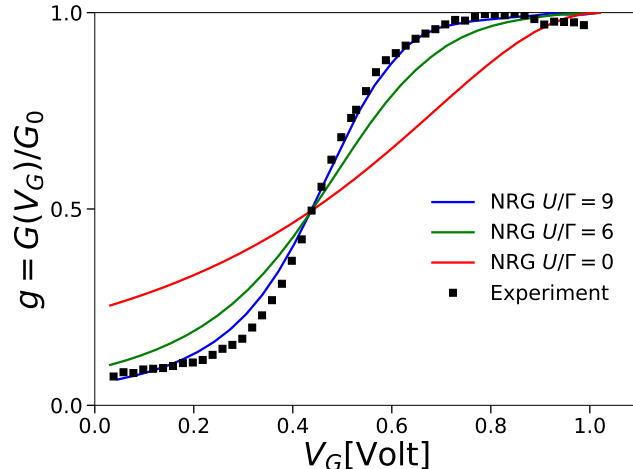


FIG. S6. Rescaled experimental conductance $g(V_G) = G(V_G)/G_0$ (black dots) as a function of gate voltage V_G in the experiment. The NRG results (colored lines), shown here for three values of $U/\Gamma = 0, 6, 9$, are shifted to match the center of the Coulomb diamond location, and are rescaled horizontally so that all NRG curves intercept the experimental data set at the diamond edge (midpoint $g = 1/2$), allowing to test the scaling form of $g(V_G)$. The optimal value $U/\Gamma = 9$ is inferred from this comparison.

CHARACTERIZATION OF SAMPLE A

The nanometric crack appearing in electromigrated constrictions after the breaking procedure has normally an irregular shape and the distance between the two resulting leads is variable along the constriction section, often below 1 nm at certain spots. Usually, a tunneling current directly from one lead to the other is measurable, bypassing any possible quantum dot and originating a conductance background. We start the characterization of the sample by measuring the linear shunt resistance of the junction, R_S , away from the degeneracy point in the even occupation side. We found $R_S \approx 20\text{ M}\Omega$ at $V_G = -0.2\text{ V}$ in sample A.

Coulomb blockade analysis

The well-known diamond like structure of blocked current regions appearing in the stability diagram of gated-quantum dot junctions become blurred in the presence of higher order transport processes (like the spin-flip Kondo resonance), enhanced due to a high relative tunnel coupling energy scale ($\Gamma \gg k_B T$). An appropriate extraction of the diamond features is crucial to determine quantitatively the relevant parameters of the quantum dot junction, such as its degeneracy point position (V_G^0) in the gate voltage dimension, its capacitive coupling to the source, drain and gate electrodes (C_S, C_D, C_G respectively) and its charging energy U . The sharp density of states of the superconducting Al leads promotes the diamond edges differential conductance, allowing us to perform linear fits of the corresponding conductance maxima, as shown in Fig. S7a. Adapting Coulomb blockade standard analysis methods [33] to our particular case of superconducting leads, the degeneracy point is found to be at $V_G^0 \approx 0.40\text{ V}$ from the middle point between the crossing of the linear fits at $V = 0$, in excellent correspondence with the mid point $g = 1/2$ at which the measured zero-bias conductance of the Kondo resonance decreases by half, providing a criterium to select the numerical values of α_G for the comparison of the NRG simulations in Fig. S6 with the experimental data. The experimental

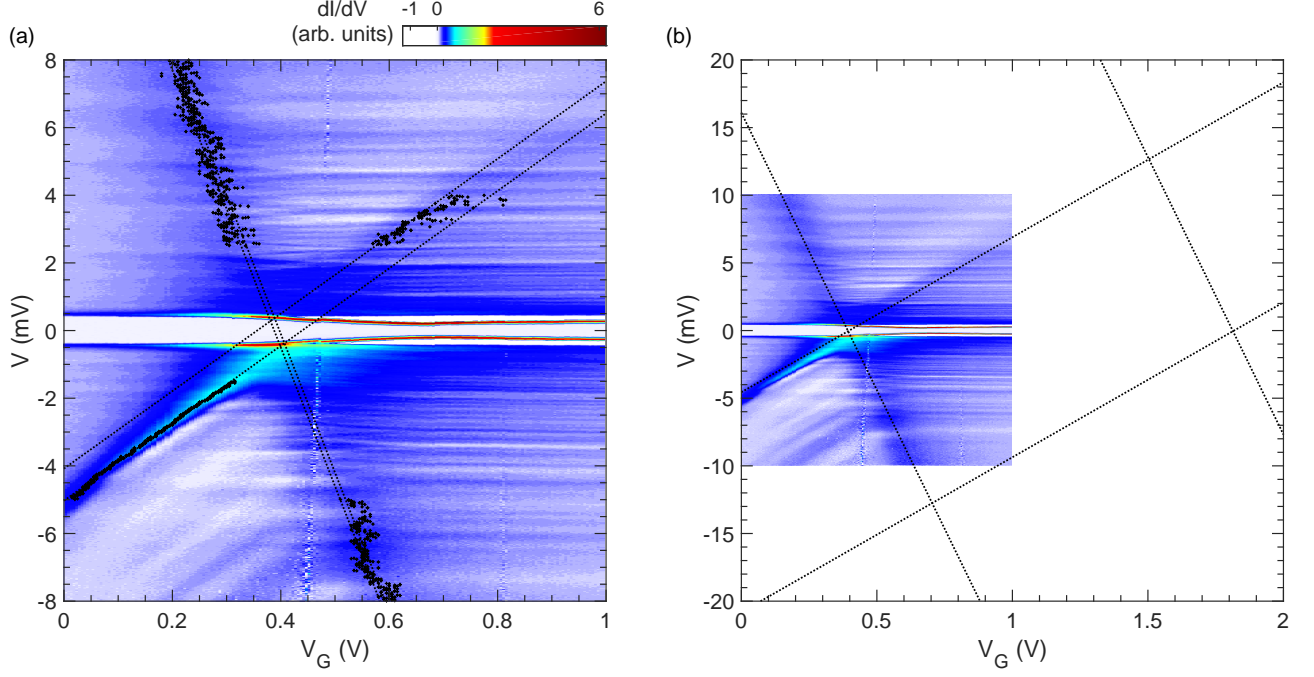


FIG. S7. (a) Superconducting state dI/dV differential conductance stability diagram of sample A. Linear fits (dashed lines) of the extracted conductance maxima (black dots) have been done to infer the four diamond edges. A certain displacement between linear fits with the same slope is introduced by the opening of a spectroscopic gap at zero V in the superconducting state (b) By plotting the linear fits obtained in (a) at the next degeneracy point ($V_G^1 \approx 1.8$ V), extrapolated from the parabolic fit in Fig. S8c, we obtain a full picture of the stability diagram allowing to extract an approximated value of $U \approx 12.7$ meV from the crossing of the linear fits at finite V .

gate lever arm α_G and the source–drain capacitance asymmetry have been determined from the extracted positive ($\beta = 11.5$ meV/V) and negative ($\beta' = -41$ meV/V) diamond edges slopes using the following relations:

$$\alpha_G = \frac{C_G}{C_S + C_D + C_G} = \frac{\beta\beta'}{\beta + \beta'} \approx 9 \text{ meV/V}, \quad (\text{S4})$$

$$\frac{C_D}{C_S} = \frac{\beta'}{\beta(1 - \beta)} \approx 3.5. \quad (\text{S5})$$

The high source–drain capacitance asymmetry derived for sample A is reflected in a few orders of magnitude difference in the tunnel couplings (calculated later in this section), leading to a probing configuration of a strongly coupled system, commonly reached in scanning electron microscopy experiments. The small α_G value, typical from single molecule/nano-particle transistors, does not allow to observe the next degeneracy point (V_G^1) of the quantum dot junction. However, as explained in the following, we performed a parabolic fit of the Kondo temperature gate dependence that indicates the position of the Coulomb diamond center V_G^{center} to be close to 1.1 V. An extrapolation of the next degeneracy point can be done so that $V_G^1 = V_G^{\text{center}} + (V_G^{\text{center}} - V_G^0) \approx 1.8$ V (see Fig. S7b), leading to a charging energy of $U \approx 12.7$ meV, in good agreement with the value found for the experimental gate coupling of around 0.9 %.

Alternative Kondo temperature extraction methods

Different criteria can be found in the literature for the experimental extraction of the Kondo energy scale (T_K) in quantum dot junctions. The lack of a general T_K definition valid for all regimes of relative energy scales complicates the fitting and comparison of results for samples involving different ratios between U , Γ and ϵ_0 . For quantum dot junctions identified to be in the Kondo regime ($U \gg \Gamma$), a possible zero-temperature definition is $T_K = 0.28\sqrt{\Gamma U}e^{-\frac{\pi U}{8\Gamma}}$, valid only at the center of the odd diamond ($\epsilon_0 = -U/2$). Although the T_K dependence remains the same [34], in a

generic electrostatic configuration within the Coulomb diamond (namely $0 > \epsilon_0 > -U$) the proportionality factor is not well-defined:

$$T_K \propto \sqrt{\Gamma U} e^{\frac{\pi \epsilon_0 (\epsilon_0 + U)}{2\Gamma U}}. \quad (\text{S6})$$

Experimentally, T_K is often extracted from the *full width at half maximum* (FWHM) of the Kondo zero-bias peak, with a variable multiplicative factor [8, 25, 29, 35–37] generally equal to 1/2. However, thermal broadening and reduction of the resonance, conductance backgrounds and slight shifts in the relative energy scales can induce a non-negligible mismatch between different experiments in Kondo-regime systems. Alternatively, an empirical expression deduced from the NRG model was proposed by Goldhaber-Gordon et. al. [38], as a rigorous method for extracting T_K , based on the universal dependence of the relative resonance maxima conductance with temperature:

$$G(T) = G_0 \left(\frac{T^2}{T_K^2} (2^{1/s} - 1) + 1 \right)^s + G_B, \quad (\text{S7})$$

where $G_0 + G_B$ represents the zero bias conductance at zero temperature (as explained in the first section), G_B represents the conductance background of the junction (typically $G_0 \gg G_B$), and s is a fitting parameter found to be around $s = 0.22$ for magnetic Kondo impurities with spin 1/2. In symmetrically coupled quantum dot junctions in the Kondo regime measured at zero temperature, $G(T \rightarrow 0) \approx G_0$ is expected to reach the quantum of conductance $2e^2/h$ around the center of the odd diamond ($-U < \epsilon_0 < 0$). In contrast, in an asymmetric case where one lead has a reduced coupling down to the so-called sequential regime ($\Gamma \gg k_B T \gtrsim \gamma$), the absence of Kondo correlations with this weakly coupled lead (γ) modulates the peak intensity of the Kondo resonance (only present at the strongly coupled lead), leading to a strong reduction w.r.t. to the unitary value:

$$G_0 \simeq \frac{2e^2}{h} \frac{4\gamma}{\Gamma^2}. \quad (\text{S8})$$

In our sample configuration, the presence of a gate electrode allows us to modify the quantum dot chemical potential ($\epsilon_0 = \alpha_G V_G$ up to an arbitrary offset at V_G^{center}), leading to a gate-tunable T_K parameter. We have measured and performed a least squares fit of $G(T)$ at different temperatures of sample A with Goldhaber-Gordon's Eq. (S7), for each accessible value of V_G (Fig. S8a).

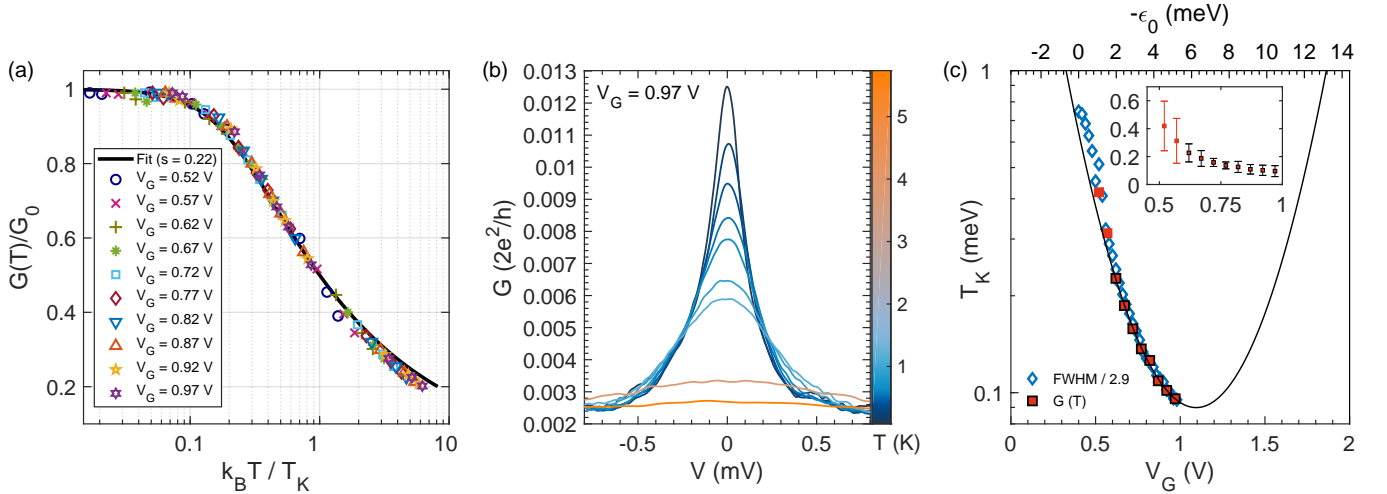


FIG. S8. (a) The temperature dependence of the zero-bias linear conductance shows an universal behavior for different V_G (ϵ_0), well described by Eq. (S7). The T_K normalizing value at each V_G have been found using a least squares fitting method. (b) Differential conductance spectroscopies of the Kondo resonance at different temperatures for $V_G = 0.97$ V. (c) The gate dependence displayed by the extracted T_K values in (a) is identical to the low temperature FWHM of the resonance (scaled by a factor of 1/2.9). A qualitative parabolic fit according to Eq. (S6) has been done for $G(T)$ data points away from the mixed valence regime (framed squares). The inset shows the same T_K values represented in linear scale, including error bars showing the standard deviation of the least squares fit.

The resulting values of T_K were found by setting $G_B = 0$ (since the differential conductance away from the degeneracy point ($V_G = -0.2$ V) decreases below 5% of G_0), and imposing an extrapolated conductance at zero

temperature of $G_0 \approx 0.013$ (Fig. S8b). Additionally, the value of G_0 can be plugged in Eq. (S8), leading to a tunnel coupling asymmetry of $\Gamma \approx 300\gamma$. Combining the conclusions obtained from NRG simulations for the relative energy scales value of $U/\Gamma = 9$ with the extraction of $U \approx 12.7$ meV from the Coulomb blockade analysis, we derive the tunnel couplings to be $\Gamma \approx 1.4$ meV and $\gamma \approx 5 \mu\text{eV}$.

The Kondo resonance FWHM, measured as a function of bias voltage and at a base temperature of $T = 100$ mK ($k_B T = 8.6 \mu\text{eV}$), displays an identical gate-driven renormalization, albeit for a scaling factor of $1/2.9$ w.r.t. to the previous temperature-based extraction (Fig. S8c). The natural logarithm of the extracted T_K displays a clear parabolic dependence that can be fitted with the previously given T_K definition in Eq. (S6), using the extracted value for α_G to determine $\epsilon_0(V_G)$. This quadratic fit provides an alternative way of extracting the energy scales U and Γ , obtaining $U = 12.5$ meV and $\Gamma = 2.5$ meV respectively. Although the resulting U is extremely close to the value inferred from the Coulomb Blockade analysis (12.7 meV), this sample is not deep enough in the Kondo regime, as derived from the NRG simulations ($U = 9\Gamma$), so that the quadratic fit can be only taken into account qualitatively. However, the overall tendency of T_K variation with V_G is well described by the fitting parabola, leading us to designate the center of the blocked diamond (V_G^{center}) employed in the Coulomb blockade analysis from its minimum at about 1.1 V. As V_G approaches V_G^0 , the system enters into the mixed valence regime ($|\epsilon_0| \lesssim \Gamma$), where Eq. (S6) is not valid anymore and the tendency of the T_K gate dependence changes. Although the least squares fitting method still provides a normalizing T_K value for voltages of $V_G = 0.52$ V and 0.57 V, and the temperature dependence of the experimental data follows the universal behavior in rather good agreement, we observe in the inset of Fig. S8c (where T_K is represented linear scale) that the standard deviation suffers a sudden increase, reaching values around 0.2 meV. Therefore, the corresponding T_K values (shown in Fig. S8c as unframed squares) cannot be highly trusted, and have not been taken into account for fitting the parabola.

Magnetic field behavior in the superconducting state

When turning the strongly coupled lead into the superconducting state, Yu-Shiba-Rusinov (YSR) subgap excitations emerge from the competition between the superconducting electron pairing (Δ) and the Kondo correlations induced by the oddly-occupied quantum dot [8], probed at different V_G by the weakly coupled lead, which is also in superconducting state. As discussed in the main article, the crossing of the YSR resonances at zero energy indicates

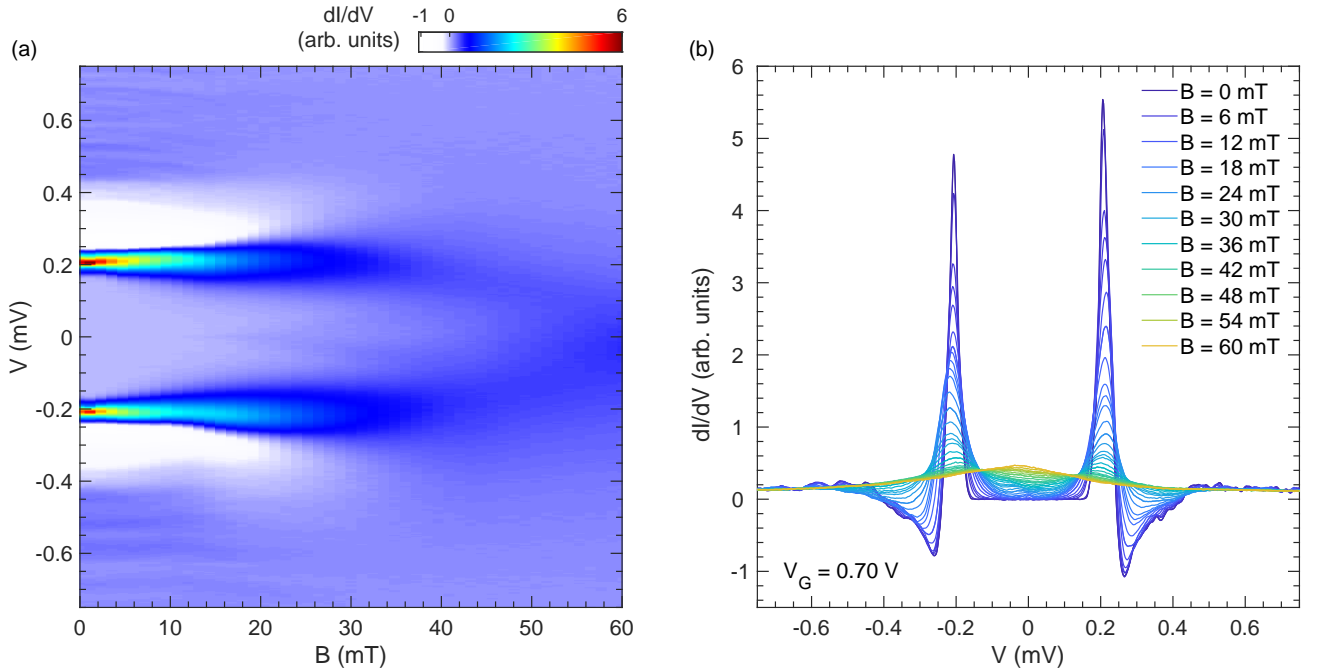


FIG. S9. (a) dI/dV differential conductance map for different values of the magnetic field at $V_G = 0.7$ V. A gradual transition from the subgap YSR states to the zero-bias Kondo resonance takes place in the spectra as magnetic field quenches superconductivity in the leads. (b) Line cuts of the map showing the spectrum evolution for increasing magnetic fields.

a phase transition happening at $T_K/\Delta \approx 0.7$ (at a critical gate voltage value of $V_G^c = 0.71$ V), where both of the ground states at each side of the critical point (the Kondo singlet at the 0-phase and the unscreened doublet at the π -phase) undergo an inversion, becoming the excited state at the contrary side.

By applying an external magnetic field (B) perpendicular to the sample surface, it is possible to quench superconductivity, turning the leads into the normal state, suppressing the superconducting energy scale Δ . In Fig. S9 we can observe how the spectroscopic gap (with a total range of $V \approx \pm 0.45$ mV at $B = 0$ mT) decreases as B is increased, and has completely disappeared at $B = 50$ mT. Accordingly, the YSR peaks decrease their intensity and finally merge into the Kondo resonance at zero bias, much broader and less intense. Tuning the gate to 0.70 V, close to the critical point (at $V_G^c = 0.71$ V), and measuring the spectrum at different B , a gentle oscillation in the energy of the negative bias YSR peak can be observed, as shown in the zoomed-in graph of Fig. 3d in the main article. In order to further investigate this phenomenon, we measured whole differential conductance maps (analogous to that one shown in Fig. S7a) at different fixed values of B . The critical gate position V_G^c displays an apparent oscillation, reaching a minimum value at 9 mT. This downwards tendency, enlarging the π -phase effective area is a consequence of the Zeeman splitting of the excited state at the 0-phase, that displaces the phase boundary position. For increasing B above 9 mT, the quenching of superconductivity in the lead gradually reduces the effective Δ , favoring the dominance of the 0-phase, i.e. the formation of the Kondo singlet.

ANDREEV BOUND STATES DISPERSION FROM RENORMALIZED PERTURBATION THEORY

In presence of superconductivity, we supplement the Anderson impurity model (S1) with a pairing contribution in the electrodes: $H_{\text{pair}} = -\sum_{k\alpha} \Delta_\alpha c_{k,\uparrow,\alpha}^\dagger c_{-k,\downarrow,\alpha}^\dagger + \text{h.c.}$, with $\Delta_{L/R}$ the superconducting gap in the left and right lead respectively. In order to gain some insight, we discuss first briefly the large gap solution of the superconducting Anderson model [29, 39–41], and make as previously the assumption of asymmetric tunneling, $\Gamma \gg \gamma$. The bare Green's function of the dot indeed becomes purely local for $\Delta_{L/R} \rightarrow \infty$ (we use here Nambu notation):

$$G_0(i\omega) = \begin{pmatrix} i\omega - B - \epsilon_0 & \Gamma \\ \Gamma & i\omega - B + \epsilon_0 \end{pmatrix}^{-1}, \quad (\text{S9})$$

which derives from an effective local Hamiltonian

$$H_{\text{eff}}^0 = \Psi^\dagger \begin{pmatrix} B + \epsilon_0 & -\Gamma \\ -\Gamma & B - \epsilon_0 \end{pmatrix} \Psi, \quad (\text{S10})$$

to which one can add the interaction term controlled by the Coulomb repulsion U . Diagonalizing the full local Hamiltonian using a Bogoliubov basis transformation provides four discrete Andreev eigenstates with the eigenvalues:

$$E_\sigma = \sigma B, \quad E_\pm = U/2 \pm \sqrt{\xi_0^2 + \Gamma^2}, \quad (\text{S11})$$

where E_σ correspond to spin polarized singly occupied states, while E_\pm are proximity induced superpositions of the empty and doubly occupied states (BCS-like states). We have noted $\xi_0 = \epsilon_0 + U/2$, the level position relative to the particle-hole symmetric point. A phase transition is readily seen to occur (for $B > 0$) when $E_\downarrow = E_-$, which reads explicitly:

$$(U + 2B)^2 = 4\Gamma^2 + 4\xi_0^2. \quad (\text{S12})$$

Thus, in absence of Kondo correlations, U and B play a similar role in determining the phase boundary, as both tend to induce a transition to a spin-polarized state, the π -phase. In most practical situations, the gap is not the largest scale in the problem, and the approximate large gap Andreev spectrum (S11) misses several physical effects, such as level repulsion at the gap edge, and the competition with the Kondo screening process. Both mechanisms are readily accounted for by a renormalized perturbative approach around the large gap limit, that we briefly introduce here [31, 42]. We first define the bare (in the large gap limit) Andreev excitation energy $a_\sigma^0 = E_- - E_\sigma$. The full transition excitation spectrum reads within renormalized perturbation theory:

$$a_\sigma = a_\sigma^0 + \delta a_\sigma = a_\sigma^0 - \frac{\Gamma}{\pi} \int_0^D d\epsilon \left[\sum_{\sigma'} \frac{1}{E - a_{\sigma'}^0 - \Theta[-\delta a_{\sigma'}] \delta a_{\sigma'}} - \frac{1}{E + b_\sigma^0} - \frac{1}{E + a_\sigma^0} \right. \\ \left. + \frac{2\Delta}{E} \frac{\Gamma_D}{\Gamma_D^2 + \xi^2} \left(\sum_{\sigma'} \frac{1}{E - a_{\sigma'}^0 - \Theta[-\delta a_{\sigma'}] \delta a_{\sigma'}} - \frac{1}{E + b_\sigma^0} + \frac{1}{E + a_\sigma^0 + \Theta[\delta a_{\sigma'}] \delta a_{\sigma'}} \right) \right] + \frac{2\Gamma_D^2}{\Gamma_D^2 + \xi^2}, \quad (\text{S13})$$

with the quasiparticle energy $E = \sqrt{\epsilon^2 + \Delta^2}$, and Θ the Heaviside function. Due to the finite bandwidth of the leads, one introduces a generalized hybridization parameter $\Gamma_D = \frac{2}{\pi} \arctan(D/\Delta)\Gamma$. Since we assumed a tunneling geometry, $\Gamma \gg \gamma$, only the single gap Δ_L of the most coupled electrode, denoted Δ , appears above. Solving for δa_σ in Eq. (S13) provides the wanted Andreev dispersion, allowing to locate the quantum phase transition when $a_\sigma = 0$ as a function of the various parameters of the system.

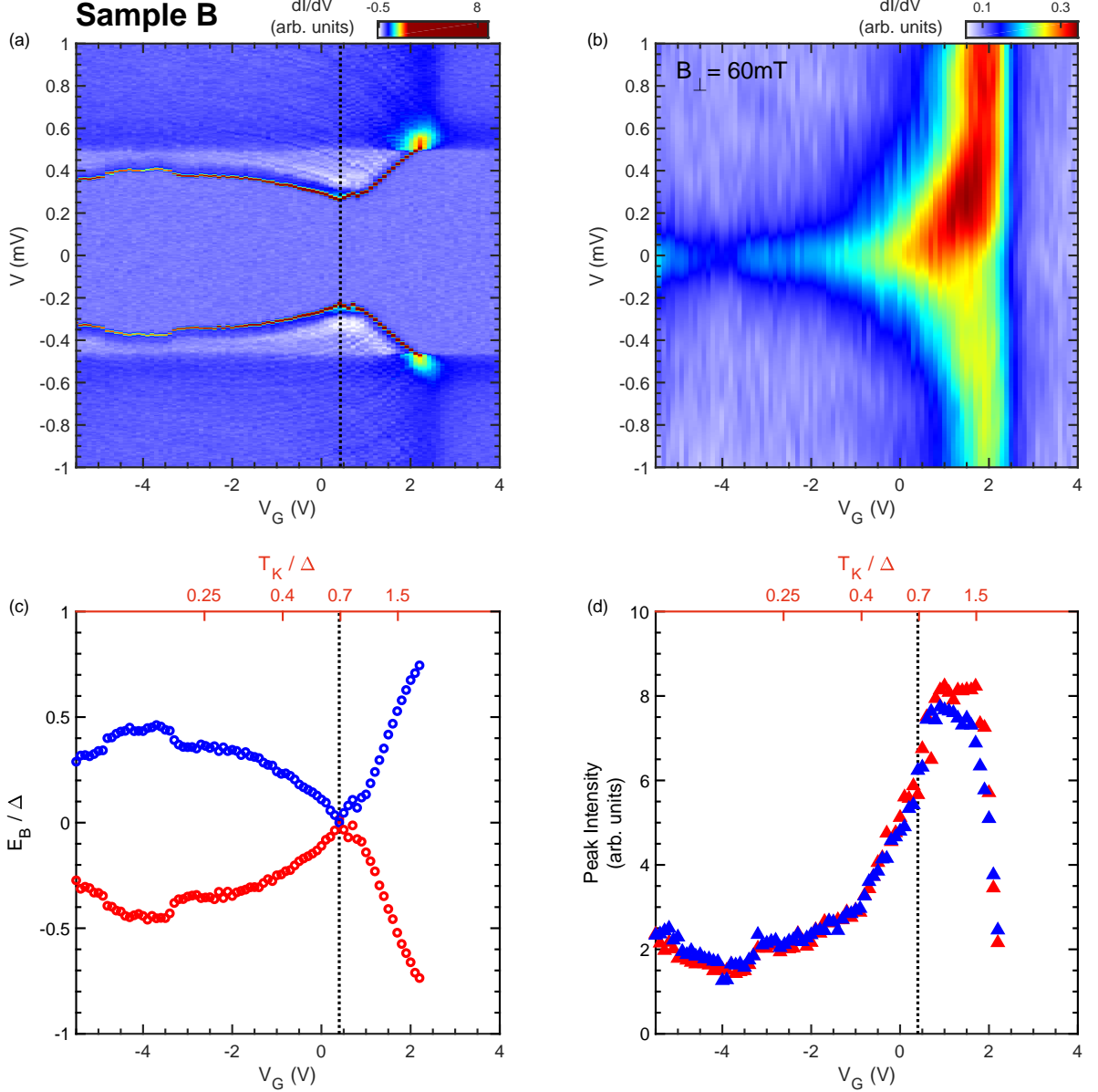


FIG. S10. (a) Superconducting state dI/dV differential conductance map of sample B. The minimal spacing of YSR spectral peaks happens at $V_G \approx 0.4$, signaling the position of the phase transition, indicated by a vertical dashed line. (b) Normal state dI/dV differential conductance map of sample B. The degeneracy point is located around $V_G \approx 2$ V. (c) YSR states' energy dispersion E_B plotted versus V_G and the corresponding Kondo energy scale T_K axes. The occurrence of the phase transition is observed at $T_K/\Delta \approx 0.7$ (d) Dependence of the YSR states' peak intensities with V_G and T_K .

CHARACTERIZATION OF SAMPLE B

Following the same headlines as in sample A, the characterization of sample B starts with the measurement of a linear shunt resistance of $15 \text{ M}\Omega$ at $V_G = 4 \text{ V}$, deep in the even diamond. Values for the superconducting pairing energy of the probing ($\Delta_{probe} \approx 240 \text{ }\mu\text{eV}$) and the strongly coupled lead ($\Delta \approx 330 \text{ }\mu\text{eV}$) have been extracted from the differential conductance map in the S state (Fig. S10a) following the same criteria as in sample A. Such an increase of the superconducting gap size in thin aluminum films with respect to the usual bulk value has been previously reported and explained as a consequence of confinement effects and granularity, [43–45] and has been commonly observed in several of our Al electromigration junctions. A more stable gate enables us to map the sample over a larger range of ϵ_0 . For instance, the conductance map in the N state (Fig. S10b) shows the zero-bias Kondo resonance developing at the degeneracy point of the quantum dot (situated at $V_G^0 \approx 2 \text{ V}$) and reaching a minimum intensity at $V_G \approx -4 \text{ V}$, indicating the center of the odd diamond, and corresponding to the maximum of the YSR states' energy dispersion in the π -phase. The complete concealment of the less intense diamond edges, buried below the Kondo-enhanced ones, makes the analysis of the diamond features and the extraction of α_G impossible in this sample.

According to the results obtained for the Kondo energy scale extraction in sample A, we give an experimental definition of T_K as the FWHM/2.9 of the Kondo resonance, this time subtracting the differential conductance background, taken as the average conductance measured between $V = \pm 0.5$ to $\pm 1 \text{ mV}$. By extracting the YSR states' energies and replacing V_G axis with the corresponding T_K non-dimensionalized with the extracted Δ , we find the occurrence of the phase transition at $T_K/\Delta \approx 0.7$ (Fig. S10c), analogous to sample A. This result points toward a similar ratio of U/Γ in this sample, which is not striking since we employed the same nano-particles colloidal solution in the fabrication of both samples, displaying a small size-distribution $>10 \%$ (leading to similar U values). The nano-particles functionalizing ligands (dodecanethiol) may pose a limit for the minimum distance between the nano-particle and the lead, or in other words, the tunnel coupling Γ . A relatively higher Kondo-enhanced diamond edge w.r.t. the zero-bias resonance, together with a sharp decrease of the YSR peak intensity across the phase transition (Fig. S10d) may point towards a larger tunnel coupling of the quantum dot to the probing electrode, becoming more sensitive to differences in the refilling rate at both sides of the phase transition.

Faint resonances displaying the same energy dispersion and V_G dependence of the YSR peaks can be observed in Fig. S10a at higher energies, appearing both inside the spectroscopic gap and also merging into the quasi-particle continuum. A hypothetical spiky density of states above Δ_{probe} in the probing lead (maybe caused by nanostructuration and granularity of the Al at the constriction) can result in low intensity replicas of the YSR resonances at higher energies.